Low SWaP, commercially-available Geiger-mode lidar system

Brandon R. Call[a], David Kelley[a], Dale G. Fried[a], Christopher Reichert[a], Kimberly Reichel-Vischi[a], and Andrew Eldredge[a]

[a]3DEO, Inc., 106 Access Road, Norwood, MA, 02062 USA

ABSTRACT

Photon-sensitive lidar receivers enable range measurements at high probability of detection and low false alarm rate using only 5 - 10 detected photons on average per range measurement. This much-reduced link requirement, compared to photodiodes operating in linear mode, holds the promise of much-reduced system volume, mass, and power consumption, while simultaneously enabling longer standoff and higher measurement rates. We present a commercially-available, Geiger-mode lidar system, called Zion, optimized for rapid collection of dense 3D point clouds using small, economical aircraft. The system mass is under 120 kg and it consumes under 1 kW. Zion has operated at ranges between 800 m and 8,000 m. The area collection rate for data products with density of 100 points per square meter exceeds 300 km^2/hr at an aircraft altitude of 1,400 m. The maximum usable measurement rate exceeds 10 million points per second. A significant capability of Zion is the agile geo-referenced scanning system, which can point and scan anywhere within a 40 $\times$ 40 degree field of regard. Collection efficiency is optimized by scanning only the desired geographic region of interest (e.g. meandering roads and utility corridors) and even in spite of non-ideal aircraft flight path and attitude. The agile, geo-referenced scanning allows the flexibility to maximize oblique imaging of structures or to penetrate dense foliage. The collected points are spread evenly across the imaged area, which reduces image artifacts and simplifies processing. This system has flown over 50 flights, and is currently operational.

Keywords: Geiger-mode, airborne, lidar, photon-timing, photon-counting, ladar, mapping, commercialization, single-photon

1. BACKGROUND: GEIGER-MODE LIDAR

The distinguishing feature of so-called "Geiger-mode" lidar systems is that the receiver detects and digitally time-stamps received photons individually. Three primary advantages of Geiger-mode systems result:

- **Link:** only 5 - 10 photon detection events are required on average to achieve high probability of detection, even in the presence of modest background noise
- **Collection rate:** modern systems use large arrays of detectors operating in parallel on each laser pulse
- **Flexibility:** collection of the signal can be distributed over many laser pulses and processing can employ sophisticated algorithms

Photon-counting lidars were used in the early 1970s for lunar ranging.[1–3] Application of photon-counting lidar to mapping was proposed in 1996.[4] A critical technological breakthrough was the integration of 2D arrays of Geiger-mode avalanche photodiodes (GmAPD's) with digital timing circuitry into compact focal plane arrays. A patent was issued[5] and much initial work was done at MIT Lincoln Laboratory.[6] Development of airborne Geiger-mode lidar systems and processing for defense and security applications has been documented elsewhere.[7–15] Geiger-mode cameras are commercially available.[16] Harris Corporation built the first airborne Geiger-mode lidar for commercial purposes.[10]

This paper describes a compact airborne Geiger-mode lidar mapping system optimized for medium-altitude mapping at high point densities. Applications include penetrating dense foliage, mapping corridors at high resolution, and mapping cities at high resolution while simultaneously mitigating shadowing effects. The system utilizes a flexible scanning system so that operators can independently control collection parameters and operate the system optimally, thereby realizing the advantages of Geiger-mode technology.

Corresponding author:DGF
E-mail: dale.fried@3deolidar.com, Telephone: +1-781-999-3447

1.1 Relation to linear-mode lidars

The required signal levels for Geiger-mode systems are much lower than signal levels for so-called "linear-mode" systems. Physics dictates a minimum average number of photon detection events that must occur in order to reliably perform a range measurement to a given range precision at a given probability of detection and false alarm rate. While in theory one needs only a few (e.g. 5) photon detection events to achieve high probability of detection and low false alarm rates,[17] for typical operational airborne Geiger-mode lidar systems[10,18] the nominal number of photon detection events per resolution element is on the order of 10, corresponding to 40 photons incident on the detector for typical photon detection efficiencies of 25%. In contrast, the sensitivity of a representative commercial linear-mode lidar system[19] is quoted as 300 photons per pulse for a probability of detection of 95% at an unspecified false alarm rate and range resolution. Systems are typically operated at signal levels of 10^4 – 10^5 photons incident on the receiver per pulse in order to provide acceptable performance over a wide range of scene and operating conditions. Because Geiger-mode systems can be operated with an optical link on the order of 10 dB lower than linear-mode systems, they are especially interesting for operation at long ranges, when minimizing size, weight, and power (SWaP), or when limited by eye safety concerns. However, the 10 dB link advantage can be easily lost if the system is not operated optimally.

The photon digitization process is said to be "noiseless", meaning that amplitude noise is not added to the signal. Remaining noise sources include false signals due to dark counts, background light, and crosstalk, and timing errors due to timing quantization and jitter. The noiseless digitization process allows signals from many individual photon detection events to be combined in post-processing using a variety of aggregation and estimation algorithms. This flexibility also enables a variety of data collection modalities and system design trades. The photon detection events can be realized over many laser pulses, over many different detector array elements (pixels) as the system scans, over varying relative geometries of the scene and sensor, and over time scales extending to weeks. In contrast, a typical linear-mode lidar must be operated so as to receive enough optical signal to exceed the receiver noise floor on a single pulse. This constraint limits the performance and utility of linear-mode systems at high altitudes or when poking through dense canopy.

1.2 Terminology

In this paper, focused on Geiger-mode lidar for mapping applications, we separate the concepts of spatial resolution, post spacing, and point density. Spatial resolution δ refers to the minimum separation required to differentiate closely spaced objects when plenty of signal is available, and is an intrinsic property of the sensor system. The spatial resolution is often specified separately as range resolution δ_z, which is independent of range and typically given as a distance, and cross-range resolution δ_θ, typically given as an angle. A post spacing b is chosen for processing, and is related to the intended average distance between points in the final output product for an unobscurred horizontal surface. De-noising and surface estimation algorithms often rely on post spacing and the 3D spatial resolution as input parameters, indicating how large of an area over which to aggregate raw photo-detection events. Data collections are typically planned to achieve an intended product post spacing with few voids. Point density σ is the number of reported points in the data product per unit area on the ground. Depending on the signal level achieved in the collection and the number of surfaces over which the signal is distributed, the achieved point density may vary over a target area and may be significantly larger or smaller than the nominal value $\sigma_{nom} = 1/b^2$. In short, spatial resolution is an intrinsic property of the sensor system, post spacing is a control parameter for the processing, and point density is a quality assessment measure of what was produced by the processing in the final product. As a scanned imaging system with photon-counting detectors, there is flexibility in how the individual photon-detection events are processed into the final product.

Several authors[17,20,21] have reported statistical analyses of the detection process relevant to Geiger-mode lidars. A good rule of thumb is that to have have a high probability of detection for a real surface in the presence of moderate background (noise) levels, the optical link and collection execution should result in at least $N_{det,req} = 8$ signal photons from the surface. If range precision is to be improved by a factor of n by averaging range measurements, a rule of thumb is that at least n^2 signal photon detections are required.[22] Geiger-mode systems typically utilize short laser pulses and high-precision, low-jitter readout electronics so that such averaging is not necessary to meet range resolution requirements. Geiger-mode lidars can measure the reflectivity of a surface; modern processing algorithms report an estimate of the reflectivity using knowledge of

the link and the statistics of the photon-detection events. The uncertainties of these estimates are impacted by shot noise. When high-confidence reflectivity estimates are required, the system must be operated so as to record larger numbers of photo-detection trials and events from the surfaces in question.

2. ZION: A LOW-SWAP GEIGER-MODE LIDAR MAPPING SYSTEM

We have developed an airborne Geiger-mode lidar mapping system optimized for collecting high point densities from medium altitudes. The system is named Zion in reference to the rugged terrain in Zion National Park in the western United States. In this section we describe the design and components of the system. In section 3 we describe the measured performance of the system. Section 4 covers the operational area collection capabilities of the system.

Zion is designed for applications that benefit from a high density of photo-detections and a high degree of angular diversity such as urban mapping and foliage penetration. In these applications, fully-detailed imagery should be collected from a large number of viewpoints so as to mitigate shadowing by forest canopy or by building walls and protrusions. Figure 1 shows example imagery collected by the Zion lidar of a school building. The sides of the buildings and utility poles are well-defined in the imagery owing to the angular diversity and high point density of the collection.

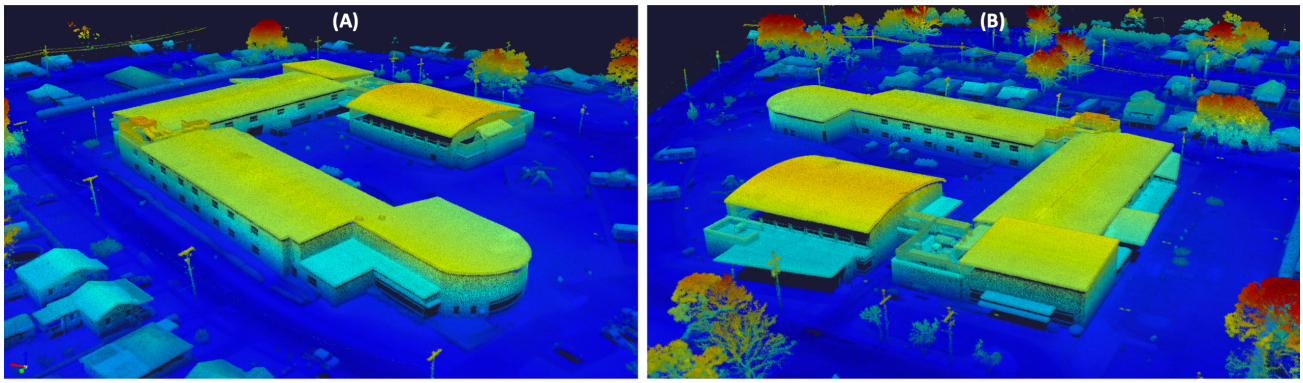

Figure 1. Two-dimensional views of a point cloud generated by the Zion lidar system and associated processing workflow. The two panels are views from the north (panel A) and south (panel B), showing good wall definition on opposite walls of the buildings. The color scale indicates elevation, ranging from -32 m to -9.7 m. The scene is at 29.9591 N, 89.9993 W. The imagery was collected March 25, 2022 from aircraft altitude of 3,000 ft. A spotlight collection mode was used, collecting an area of diameter approximately 340 m with 10 scans of the area on each of two passes. The total data recording time was 26 seconds. The resulting area collection rate was 3.3×10^3 m^2/sec (12 km^2/hr).

The Zion lidar is produced in two variants, summarized in Table 1. The Zion-A system utilizes a single Geiger-mode camera and a 15-W laser. The Zion-B system doubles the measurement rate by utilizing two Geiger-mode cameras and a 35-W laser. The laser operates at 1064.25 nm with spectral line width less than 0.2 nm, allowing use of a narrow-band spectral filter on the receiver. The pulse width varies with pulse repetition frequency from 500 ps FWHM at 50 kHz to 700 ps FWHM at 90 kHz. Beam handing optics allow the lidar output power to be adjusted continuously over two orders of magnitude. The output beam divergence is set to match the field of view of the camera detector array. The transmit beam is combined coaxially with the receive aperture, constituting a monostatic configuration.

The scanning sub-system is described in a companion paper in these proceedings.[23] The scanner enables two axes of independent motion, pointing the line-of-sight (LoS) anywhere within a field-of-regard (FoR) spanning ±20 deg in the aircraft along-track direction, and -35 deg to +5 deg in the cross-track direction. The off-center FoR was chosen to better image the sidewalls of buildings. As described by Call *et. al.*, the scanning system enables the full capability of the lidar to be concentrated on just the region of interest, defined using geographic coordinates. A "spotlight" mode repeatedly scans just a desired polygon as the aircraft flies overhead. A

Parameter	Zion-A	Zion-B	Notes
Laser power	15 W	35 W	at laser aperture
Eyesafe range (NOHD)	1070 m	1620 m	7×50 binoculars
Pulse repetition frequency	50 kHz – 90 kHz		
Number of pixels	> 4000	> 8000	
Maximum raw measurement rate (photo-detections/sec)	$2.5{\times}10^8$	5×10^8	maximum sustained recording rate of receiver system
Link: number of detected photons per second (typical)	6×10^7	1.5×10^8	Typical urban area from 2 km altitude
Pixel field-of-view	50 μrad		
Field of regard	40 × 40 deg, offset 15 deg to left		Randomly accessible

Table 1. Zion lidar hardware description. The numbers for Zion-B are scaled from observed performance of Zion-A in flight operations.

"corridor" mode scans a meandering region of configurable width as the aircraft flies a straight path. Wide-area mapping collections can be designed to achieve the intended angular diversity and sampling density.

The receiver consists of a telescope of focal length $f = 1.00$ m that images the scene onto one or more Geiger-mode cameras. The cameras have a 128×32 pixel format, and are operated synchronously with the laser at 50 kHz to 90 kHz. The overall system link results in approximately 6×10^7 photo-detections per second over typical urban areas from an altitude of 2 km for Zion-A. The link scales inversely with range squared, and can be further reduced by atmospheric attenuation. The link limits the useable measurement rate of the system, as typically collections are planned to achieve an intended number of photo-detections per post spacing in the data product. The system link is the product of the average detection probability per pixel per pulse, P_{det}, the number of pixels, N_{pix}, and the pulse repetition frequency F, as described in section 4. The detection probability for a given pixel depends on the laser pulse energy, the fraction of the laser illumination imaged by the pixel, the retro-reflectivity of the surface imaged by the pixel, details of the optical system, and the photon detection efficiency of the camera pixel. Collection planning takes account of blocking and saturation losses inherent in Geiger-mode detection so that the resulting collection has the intended density of photo-detections.

The Zion-A system prototype consists of an optical head, chiller, power supply, and operator laptop computer. The optical head enclosure ($63 \times 99 \times 52$ cm^3) contains the electronics and the optical bench assembly ($34 \times 60 \times 36$ cm^3), and weighs 98 kg. The chiller is a 3U COTS package weighing 19 kg. The power supply measures $29 \times 13 \times 4$ cm^3 and weighs 2 kg. The total system volume is 358 liters and the total system mass is 119 kg. The system draws approximately 850 W, inclusive of the chiller and control computer. Engineering efforts are underway to reduce size and mass below these prototype values.

3. SYSTEM CHARACTERIZATION

A Geiger-mode lidar system is composed of (a) the hardware that illuminates a scene and records photo-detection events; (b) the software that projects or transforms each of those events into a geolocated raw 3D point cloud, commonly called "xform"; and (c) the software used to estimate the geometry and other characteristics of the scene from that raw point cloud, commonly called a "coincidence processor". We present here measurements describing the spatial resolution of the hardware (a) alone, based on lab measurements. We then characterize the combined hardware-plus-transform system (a+b) using data from airborne collections. The flight measurements necessarily include the effects of turbulence around the aircraft, calibration, and noise in the Inertial Navigation System (INS).

The angular resolution of the hardware (a) was measured by imaging a slit of light and computing the line-spread function. The slit comprised a diffusive material back-illuminated by a near infra-red (NIR) LED lamp,

placed behind an opaque material with opening width of 0.254 mm. The slit was 33.14 m from the lidar telescope, resulting in an apparent width of 7.7 μrad. The photo-detection rate for each pixel is shown in Figure 2. The line

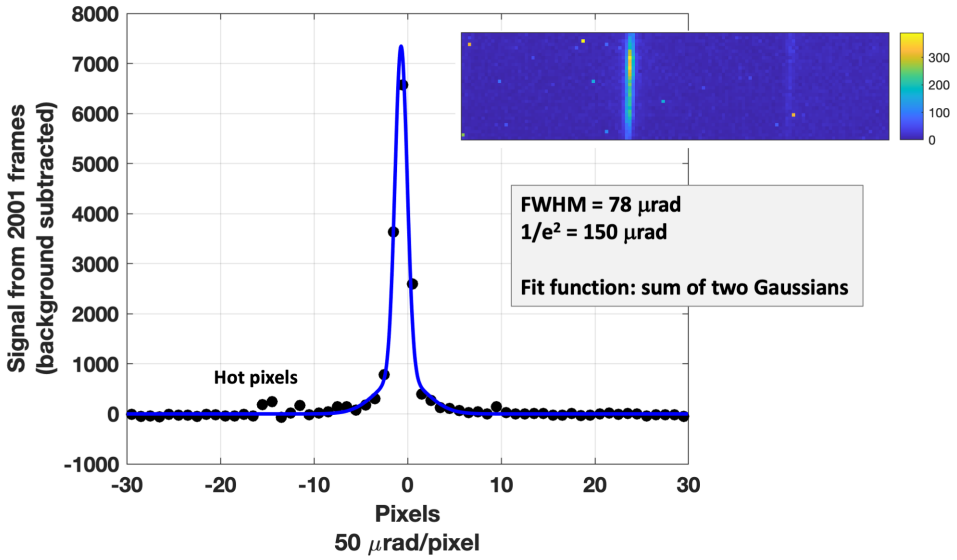

Figure 2. Lab measurement of the angular resolution of the lidar hardware. The inset shows the image of the slit on the camera. The brightest pixels fired with probability of approximately 0.2 per camera frame. The plot shows the signal aggregated from all 32 rows, with a sloping background subtracted. The data shown was collected over 40 msec. The blue curve is a best-fit of a function consisting of two Gaussians with the same center but different widths and amplitudes.

spread function was computed by applying a skew to the image to correct for the tilted slit and integrating the signals from all rows of the image. A multi-parameter minimization was used to fit a sum of two Gaussians to the data, as indicated by the blue curve in Figure 2. The FWHM is 78 μrad and the $1/e^2$ full width is 150 μrad.

The range resolution of the hardware (a) was measured by recording photo-detections from a flat plate at a distance of approximately 30.7 m from the lidar, arranged perpendicular to the line-of-sight (LoS). The measurement was done at $F = 50$ kHz, corresponding to laser pulse width of 500 ps FWHM. Data from 100,000 frames (2 sec) was used to create a range histogram for each pixel. The firing rate is defined as the probability of a pixel firing per unit time, given that it is available to fire. The pixels were partitioned into eight groups, sorted by the firing probability. The firing rate probability distribution function is similar for all but the weakest pixels, as shown in Figure 3. As indicated in the legend of Figure 3, the shift of the means from the brightest group to the seventh brightest group is only 0.18 nsec, corresponding to a range walk of 2.7 cm.

The angular resolution of the combined hardware and transform software (a+b) system was measured using flight data collected at a slant range of 1683 m. The target for the line-spread function measurement was a rope with embedded retro-reflective tape (GRIP Reflective Camo Poly Rope, 0.25-in x 50-ft; DICK's Sporting Goods), stretched taut approximately horizontally. A sample point cloud of raw photo-detections used for the analysis is indicated by the 2D image in Figure 4. The width of the nylon rope (0.6 cm) was much smaller than the ground sample distance (GSD), the projection of a pixel onto the ground, of 8.4 cm. To obtain the 1D line spread function (LSF) from the 3D point cloud we performed the following steps:

1. Crop the point cloud to a region near the rope and rotate the point cloud to align the rope to a convenient axis.

2. Find the vector $\mathbf{q}$ from each point to the nearest point on a parabolic model of the rope.

3. Retrieve the component of $\mathbf{q}$ that is perpendicular to the LoS and perpendicular to the rope, thereby giving the cross-range distance from the rope.

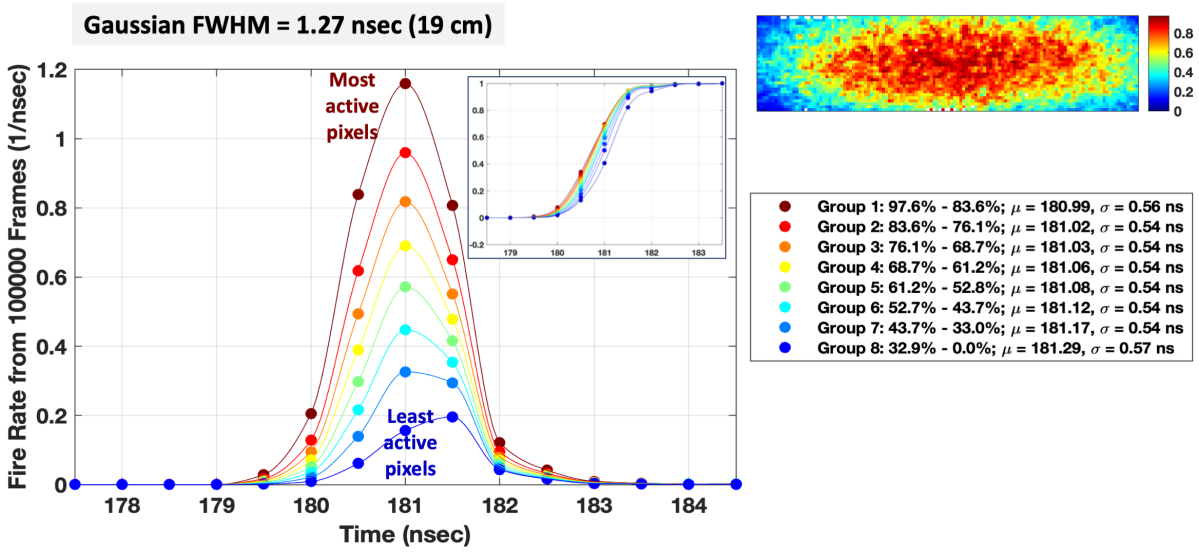

Figure 3. Lab measurement of the range resolution of the lidar hardware. The eight colors each represent a group of pixels with similar firing probability. The curves are meant as a guide to the eye. A standard deviation of 0.54 ns corresponds to a Gaussian FWHM of 1.27 nsec. The inset in the main plot shows the CDF and indicates some slight range walk. The image on the right indicates the laser illumination profile and the resulting firing probability. The legend indicates the mean μ and standard deviation σ of the data points.

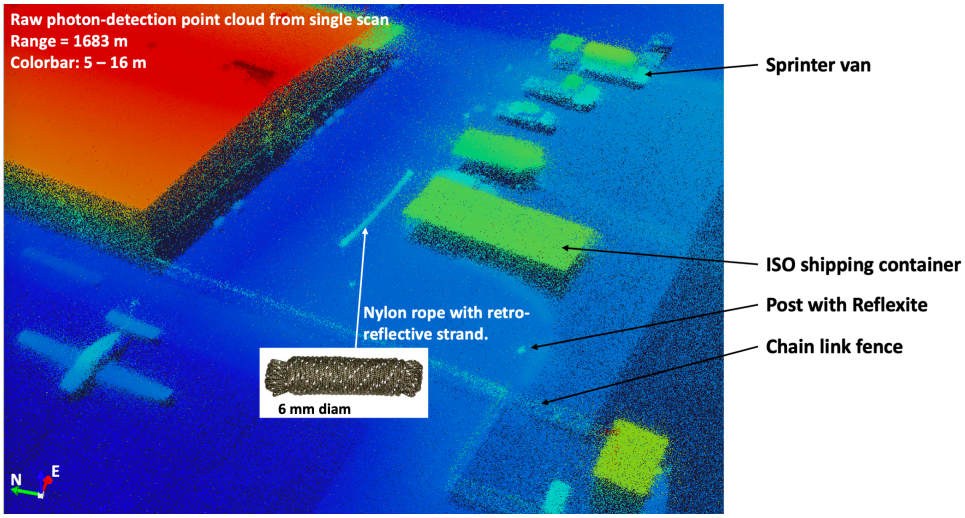

Figure 4. Representation of point cloud of raw photo-detections used for the LSF analysis.

4. Histogram the cross-range distances and fit to a function that is the sum of two Gaussians centered on the same point.

In order to gain visibility into the time scales of the physical effects causing blur, we performed these steps for each of several single swipes of the scanner across the target area, as well as for the aggregation of all the swipes comprising a scan. An example of the single-swipe distribution function is shown in Figure 5. The data contributing to the single-swipe analysis was collected over approximately 700 μsec. Over the course of a single scan of the target area, a circle of diameter 200 m, data of the LSF target originated from seven successive swipes. The swipes occurred over an interval of 68 msec, long compared to the INS update interval of 10 msec. Figure 6 shows the probability distribution function over this longer time scale. Note that the LSF PDF presented here comprises the hardware and transform software (a+b), but does not include the coincidence processing stage (c).

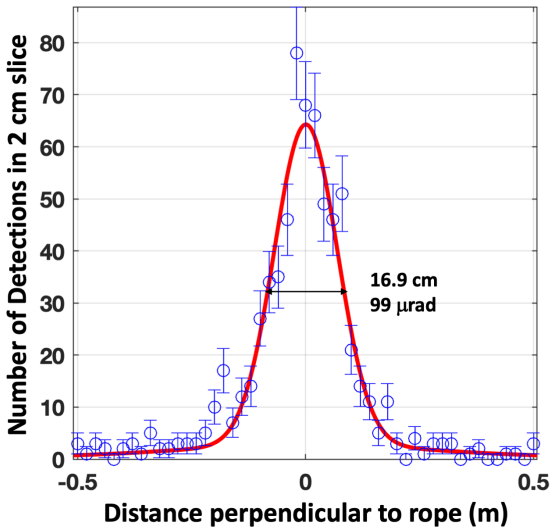

Figure 5. Line-spread function derived from a single swipe of the scanner moving the detector FoV across the scene. The distances from the rope are histogrammed in bins of width 2 cm. The errors bars are of length $\pm\sqrt{N}$, where N is the number of photo-detections in the bin, and are intended to indicate shot noise. The red curve is a best-fit sum of two Gaussians of unequal width but identical center point. The width of this curve at half its peak height is 16.9 cm, corresponding to 99 μrad at the slant range of the measurement.

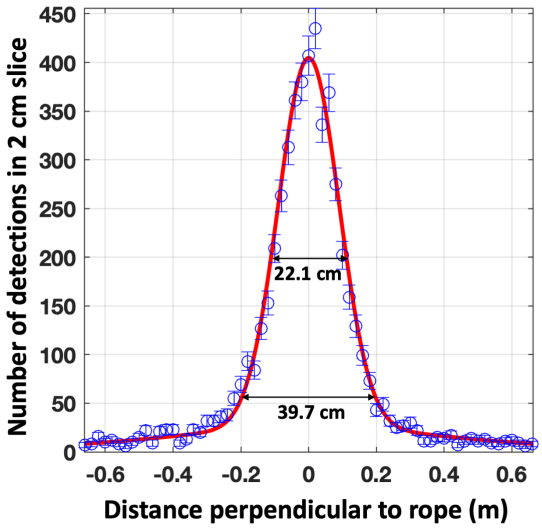

Figure 6. Line-spread function derived from seven swipes comprising a single scan of the scene. The distances from the rope are histogrammed in bins of width 2 cm. The errors bars are of length $\pm\sqrt{N}$, where N is the number of photo-detections in the bin, and are intended to indicate shot noise. The red curve is a best-fit sum of two Gaussians of unequal width but identical center point. The width of this curve at half its peak height is 22.1 cm, corresponding to 128 μrad at the slant range of the measurement.

The results indicate that, for example, two suspended wires separated by 130 μrad should be distinguishable after processing by a well-performing coincidence processor.

The range resolution of the combined hardware plus transform software (a+b) system was assessed using flight data as follows.

1. A large planar surface was identified. We chose a concrete slab that was poured as the floor of a hangar under construction. The surface slopes in one direction with a specified angle of 0.0042 radians. We chose

a sub-region (area 240 m^2) that was manually inspected. The reflectivity of the fresh concrete is expected to be approximately 30%.

2. The area was scanned as part of a larger spotlight collection of a circular area approximately 360 m in diameter. The LoS was off-nadir by approximately $\theta = 15$ deg, which is expected to introduce a range smear with standard deviation $\sigma = R\phi \tan\theta/\sqrt{12} = 1.0$ cm for slant range $R = 1000$ m and pixel ground sample resolution (GSR) $\phi = 127$ μrad.

3. The raw point cloud of photo-detections was cropped to the selected area and cropped vertically to within 1.1 m of the ground. A plane was fit to the remaining points.

4. The vertical distance from each raw point to the best-fit plane was histogrammed to show the vertical error distribution function.

The probability distribution function (PDF) and cumulative distribution function (CDF) are indicated in Figure 7. The raw photo-detection point cloud was processed using a simple coincidence processor, set to operate

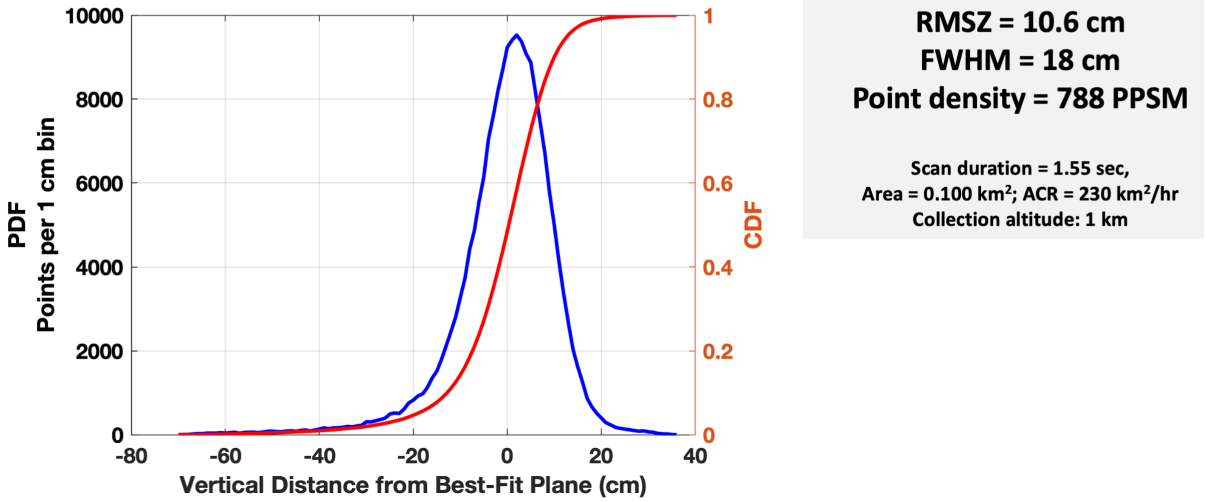

Figure 7. Distribution functions for the vertical deviations of the raw photo-detection data points from a best-fit plane.

at a post spacing of 10 cm. The vertical variation analysis was conducted for the resulting point cloud. The resulting RMS vertical variation was 5.6 cm. This result is not inconsistent with the expectation of reducing the 10.6 cm RMS variation for the raw data by a factor of $\sqrt{N}$, where $N = 7.88$ is the average number of raw detections per post spacing. In the absence of other noise sources we would have expected an RMS vertical variation of 3.8 cm. The measured range impulse response taken from the raw photo-detection point cloud is expected to indicate the ability of the system to resolve two surfaces closely-spaced in range, but unresolved angularly. The definitive demonstration will involve the third critical component of a Geiger-mode lidar, the coincidence processor.

The analysis of the performance of the hardware (a) and the combined hardware plus transform software (a+b) system provides a 3D (range and cross-range) description of the spatial resolution which is a critical input to the coincidence processor.

4. SYSTEM AREA COLLECTION RATE

The rate at which an area can be mapped or otherwise imaged by a Geiger-mode lidar system is limited primarily by three factors:

1. **Geometry** The aircraft ground speed v and the maximum cross-track angular field of regard bounded by left and right edges θ_L and θ_R define an area collection rate limit

$$\Gamma_{geom}(h) = v(h)\ h\ (\tan\theta_R - \tan\theta_L)(1-\eta) \tag{1}$$

that depends on the flying altitude above ground h and the required swath overlap fraction η. Allowances for roll margin are included in the FoR angles. Significant swath overlap (e.g. $\eta = 50\%$) is often used to achieve angular diversity and image all sides of buildings. The maximum ground speed v is often a weak function of the altitude.

2. **Signal rate** The collection is typically planned so that a desired minimum density of photo-detections is achieved on the scene. The required density

$$\sigma_{pd} = N_{det,req}\ N_{LoS}/b^2 \tag{2}$$

is derived from the required average number of detections per post spacing $N_{det,req}$, the angular diversity as quantified by number N_{LoS} of different line-of-sight angles that should be used to interrogate a given spot on the ground, and the post spacing b used in the processing. The requirements of the end user's image exploitation task and the dynamic range of the reflectivity throughout the scene set $N_{det,req}$. A typical value is $N_{det,req} = 8$ for a surface with the scene-average reflectivity. The value may be increased if it is important to reliably produce points on dark surfaces within the scene, to penetrate through heavy foliage in which the hole sizes are small compared to the angular resolution, or to produce products with low noise in the reflectivity estimate.

The area collection rate limit

$$\Gamma_{signal}(h) = \frac{N_{pixels}\ F\ P_{det}(h)}{\sigma_{pd}} \tag{3}$$

is determined by the number of pixels N_{pixels} in the system, the pulse repetition frequency F, and the average probability of detection per pixel per pulse P_{det}, which is a function of altitude, h. For the Zion-A system the detection probability is typically $P_{det} = 18\%$ at flying altitude of 2 km and $F = 90$ kHz over typical urban area. The detection probability falls as h^{-2} and is further reduced by atmospheric attenuation.

3. **Saturation and blocking** Range walk due to detector saturation can become noticeable if the firing probability becomes too high. Furthermore, when looking through partial obscurants such as forest canopy, blocking effects can become significant at higher firing probability. For these reasons the Zion-A system is typically operated no higher than $P_{det} = 35\%$. This altitude-independent limit is chosen to provide mitigation for deleterious effects. It is not a hard limit but is rather chosen based on the scene characteristics and the image fidelity requirements.

The area collection rate limits are shown graphically in Figure 8. Details are in the figure caption. Because of Zion's flexible scanning system the angular diversity can be easily configured for a given collection. The achievable point density can be distributed over many different scans if so desired. For example, the 200 PPSM indicated by the orange curve can be collected as 8 scans from different view angles, each with 25 PPSM.

5. CONCLUSION

The Zion lidar system is, to the best of our knowledge, the first Geiger-mode airborne mapping lidar available for commercial sale or lease. The system's spatial resolution and area collection rate enable substantially more efficient data collections, and therefore reduced costs, for commercially-relevant applications. We anticipate the cost effective, high density data products to have wide application as inputs to automated exploitation algorithms based on artificial intelligence and machine learning. In addition, the system can be operated at arbitrarily high altitudes, simplifying collection over regions of high terrain relief. Finally, the agile geo-referenced scanning capability further enhances collection efficiency by enabling the operator to focus the full system capability on just the regions of interest.

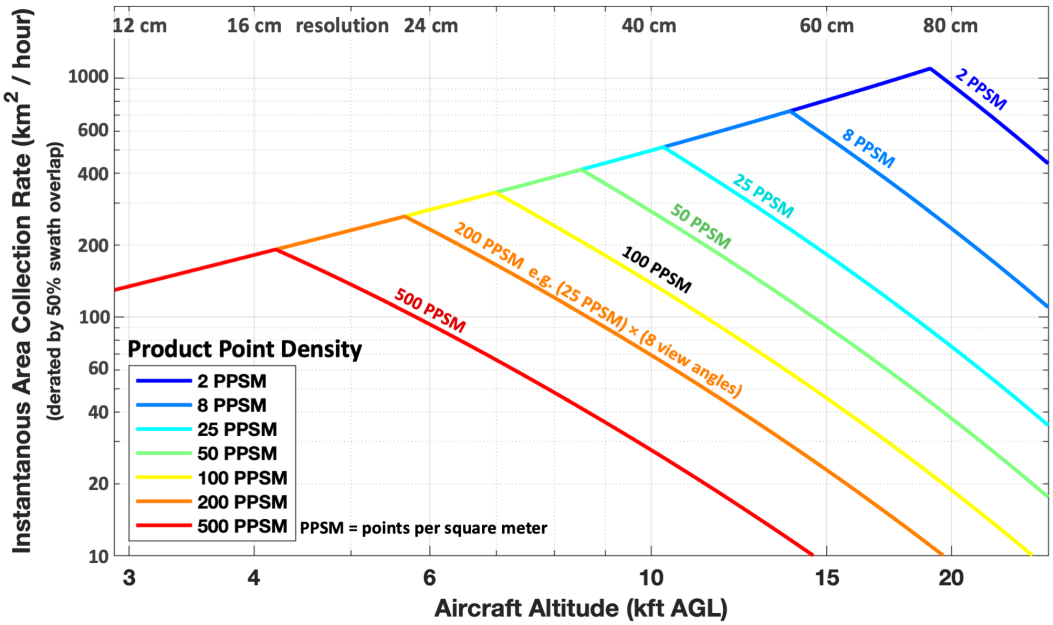

Figure 8. Achievable area collection rate for the Zion-B system as a function of flying altitude. The seven curves indicate different assumptions for the product point density N_{LoS}/b^2. At low altitudes the area collection rate is limited by the aircraft ground speed (assumed to be 230 kts indicated airspeed, a slowly-varying function of altitude) and the swath width. A swath overlap factor of $\eta = 50\%$ was assumed, and the cross-track scan limits $\theta_L = -32$ deg and $\theta_R = +2$ deg reflect roll margin of ± 3 deg. At high altitudes the area collection rate is limited by the returned signal rate. The required average number of photo-detections per LoS is $N_{ret,req} = 8$. The numbers across the top of the figure indicate the ground spatial resolution at an off-nadir angle midway between the cross-track scan limits.

REFERENCES

[1] Lehr, C. G., Pearlman, M. R., Monjes, J. A., and Hagen, W. F., "Transportable lunar-ranging system," *Appl. Opt.* **11**, 300–304 (Feb 1972).

[2] Lehr, C. G., Ouellette, J. P., Sozanski, P. W., Williams, J. T., Criswell, S. J., and Mattei, M., "Lunar range measurements with a high-radiance frequency-doubled neodymium–glass laser system," *Appl. Opt.* **12**, 946–947 (May 1973).

[3] Silverberg, E. C., "Operation and performance of a lunar laser ranging station," *Appl. Opt.* **13**, 565–574 (Mar 1974).

[4] Priedhorsky, W. C., Smith, R. C., and Ho, C., "Laser ranging and mapping with a photon-counting detector," *Appl. Opt.* **35**, 441–452 (Jan 1996).

[5] Marino, R. M., "Method and apparatus for imaging a scene using a light detector operating in non-linear geiger-mode," (Apr. 6 1999). U.S. Patent 5,892,575, issued April 6, 1999.

[6] Aull, B., "Geiger-mode avalanche photodiode arrays integrated to all-digital cmos circuits," *Sensors* **16**(4) (2016).

[7] Albota, M. A., Heinrichs, R. M., Kocher, D. G., Fouche, D. G., Player, B. E., O'Brien, M. E., Aull, B. F., Zayhowski, J. J., Mooney, J., Willard, B. C., and Carlson, R. R., "Three-dimensional imaging laser radar with a photon-counting avalanche photodiode array and microchip laser," *Appl. Opt.* **41**, 7671–7678 (Dec 2002).

[8] Vaidyanathan, M., Blask, S., Higgins, T., Clifton, W., Davidsohn, D., Carson, R., Reynolds, V., Pfannenstiel, J., Cannata, R., Marino, R., Drover, J., Hatch, R., Schue, D., Freehart, R., Rowe, G., Mooney, J., Hart, C., Stanley, B., McLaughlin, J., Lee, E.-I., Berenholtz, J., Aull, B., Zayhowski, J., Vasile, A., Ramaswami, P., Ingersoll, K., Amoruso, T., Khan, I., Davis, W., and Heinrichs, R., "Jigsaw phase III: a miniaturized airborne 3-D imaging laser radar with photon-counting sensitivity for foliage penetration," in

[*Laser Radar Technology and Applications XII*], Turner, M. D. and Kamerman, G. W., eds., **6550**, 165 – 176, International Society for Optics and Photonics, SPIE (2007).

[9] Oh, M. S., Kong, H. J., Kim, T. H., Jo, S. E., Kim, B. W., and Park, D. J., "Development and analysis of a photon-counting three-dimensional imaging laser detection and ranging (ladar) system," *J. Opt. Soc. Am. A* **28**, 759–765 (May 2011).

[10] Clifton, W. E., Steele, B., Nelson, G., Truscott, A., Itzler, M., and Entwistle, M., "Medium altitude airborne Geiger-mode mapping LIDAR system," in [*Laser Radar Technology and Applications XX; and Atmospheric Propagation XII*], Turner, M. D., Kamerman, G. W., Thomas, L. M. W., and Spillar, E. J., eds., **9465**, 39 – 46, International Society for Optics and Photonics, SPIE (2015).

[11] Henriksson, M., Larsson, H., Grönwall, C., and Tolt, G., "Continuously scanning time-correlated single-photon-counting single-pixel 3-D lidar," *Optical Engineering* **56**(3), 1 – 9 (2016).

[12] Albota, M. A., Gurjar, R., Mangognia, A., Dumanis, D., and Edwards, B., "Contributed review: Advanced three-dimensional laser radar imaging with the airborne optical systems testbed," *Review of Scientific Instruments* **89**(10), 101502 (2018).

[13] Dumanis, D., "Airborne optical systems test bed (aostb)," tech. rep., MIT Lincoln Laboratory Lexington United States (2016).

[14] Vasile, A. N., Skelly, L., Edwards, B., Stowe, L., and Khan, M. J., "Photon-counting ladar in support of disaster relief (Conference Presentation)," in [*Advanced Photon Counting Techniques XIII*], Itzler, M. A., Bienfang, J. C., and McIntosh, K. A., eds., **10978**, International Society for Optics and Photonics, SPIE (2019).

[15] Liu, F., He, Y., Yuan, L., Chen, Y., Jiao, C., Yu, J., Guo, S., Huang, Y., and Chen, W., "Airborne Geiger-mode lidar system with real-time data compression," in [*Twelfth International Conference on Information Optics and Photonics*], Yang, Y., ed., **12057**, 876 – 882, International Society for Optics and Photonics, SPIE (2021).

[16] Kondratko, P. K., Segal, S., and Aina, O. A., "Geiger-mode Avalanche Photodiode (GmAPD) arrays for single photon non-conventional imaging," in [*Unconventional Imaging and Adaptive Optics 2021*], Dolne, J. J. and Spencer, M. F., eds., **11836**, International Society for Optics and Photonics, SPIE (2021).

[17] Fouche, D. G., "Detection and false-alarm probabilities for laser radars that use geiger-mode detectors," *Appl. Opt.* **42**, 5388–5398 (Sep 2003).

[18] Knowlton, R., "Airborne ladar imaging research testbed," tech. rep., MASSACHUSETTS INST OF TECH LEXINGTON LINCOLN LAB (2011).

[19] Ullrich, A. and Pfennigbauer, M., "Linear LIDAR versus Geiger-mode LIDAR: impact on data properties and data quality," in [*Laser Radar Technology and Applications XXI*], Turner, M. D. and Kamerman, G. W., eds., **9832**, 29 – 45, International Society for Optics and Photonics, SPIE (2016).

[20] O'Brien, M. E. and Fouche, D. G., "Simulation of 3d laser radar systems," *Lincoln Laboratory Journal* **15**(1), 37–60 (2005).

[21] Milstein, A. B., Jiang, L. A., Luu, J. X., Hines, E. L., and Schultz, K. I., "Acquisition algorithm for direct-detection ladars with geiger-mode avalanche photodiodes," *Appl. Opt.* **47**, 296–311 (Jan 2008).

[22] Pellegrini, S., Buller, G. S., Smith, J. M., Wallace, A. M., and Cova, S., "Laser-based distance measurement using picosecond resolution time-correlated single-photon counting," *Measurement Science and Technology* **11**(6), 712 (2000).

[23] Call, B., Fried, D., Kelley, D., and Reichert, C., "Dynamic geo-referenced scanning of aerial lidar systems," International Society for Optics and Photonics, SPIE (2022).